A Learning-Based Physical Model of Charge Transport in Room-Temperature Semiconductor Detectors

Srutarshi Banerjee, *Graduate Student Member, IEEE*, Miesher Rodrigues, *Member, IEEE*, Alexander Hans Vija, and Aggelos K. Katsaggelos, *Life Fellow, IEEE*

***Abstract*— Room-temperature semiconductor radiation detectors (RTSDs) such as CdTe are becoming popular in computed tomography (CT) imaging. These detectors are often pixelated, requiring cumbersome postinteraction 3-D event reconstruction, which can benefit from detailed material characterization at the micron level. Transport properties and material defects with respect to electrons and holes are to be characterized, which is a labor-intensive process. Current state-of-the-art characterization is done either as a whole or at most pixel-by-pixel over the detector material. In this article, we propose a novel learning-based physical model to infer material properties at the microscopic level for RTSD. Our approach uses a novel physics-inspired learning model based on physical transport of charges with trapping centers for electrons and holes in the detector. The proposed model learns these material properties from known or measured input charges to the detector along with known or measured output signals and distributed charges in the bulk of the RTSD. The actual physical detector is divided into voxels in space and takes into account different material properties (such as drift, trapping, detrapping, and recombination) in each voxel as learnable model parameters. The model is based on a physics-inspired recurrent neural network model instead of traditional convolutional or fully connected networks. The advantage of our approach is the one-to-one relationship between the actual physical parameters of the voxels and learnable weights in the model, far fewer trainable parameters compared to traditional neural network approaches and less training time. The performance of our model has been evaluated on cadmium zinc telluride (CdZnTe), with voxels of three sizes, 25, 50, and 100 μm, for single charge input as well as multiple charge inputs at different voxel positions. Our learning-based model provides material properties with higher spatial resolution and performs well in all scenarios and matches the actual physical parameters better than state-of-the-art classical approaches.**

***Index Terms*— Charge transport, defects, detrapping, learning-based model, material characterization, room temperature semiconductor detector, Schokley–Ramo theorem, trapping, trapping centers.**

Manuscript received July 2, 2021; revised October 18, 2021; accepted November 12, 2021. Date of publication November 23, 2021; date of current version January 19, 2022. This work was supported by Siemens Medical Solutions USA, Inc.

Srutarshi Banerjee and Aggelos K. Katsaggelos are with the Department of Electrical and Computer Engineering, Northwestern University, Evanston, IL 60208 USA (e-mail: srutarshibanerjee2022@u.northwestern.edu; a-katsaggelos@northwestern.edu).

Miesher Rodrigues and Alexander Hans Vija are with Siemens Medical Solutions USA Inc., Hoffmann Estates, IL 60192 USA (e-mail: miesher.rodrigues@siemens-healthineers.com; hans.vija@siemens-healthineers.com).

Color versions of one or more figures in this article are available at https://doi.org/10.1109/TNS.2021.3130486.

Digital Object Identifier 10.1109/TNS.2021.3130486

I. Introduction

ROOM-TEMPERATURE semiconductor radiation detector (RTSDs) are used for diverse applications in X-ray and γ-ray detection systems such as homeland security and computed tomography (CT) medical systems [1]–[3]. The desired characteristics of RTSD are high quality crystal with uniform and optimized charge transport properties—with no polarization effect, excellent fabrication quality, high breakdown voltage, high charge transport speeds, and high energy resolution. RTSDs have high stopping power due to high density, high atomic number and can operate at high voltages due to their high resistivity and contact engineering, which has led to their wide applicability compared to detectors such as Si and high purity germanium (HPGe). Recently, RTSD manufacturers have developed high-flux material [4], which promise to address the space charge polarization issues. RTSDs are often used as compact radiation detection units with highly segmented pixelated anode patterns. Pixelated cadmium zinc telluride (CdZnTe) detectors have been used in pulse mode at high-fluxes [5], [6]. Recently, the high performance of CdZnTe has been shown at room-temperatures.

Despite recent advances in RTSD's properties, the repeatability of its properties across multiple detectors and within a detector is unknown. Previous measurements with large-area CdZnTe and CdTe detectors have demonstrated spatial variations in the detector response due to crystalline defects such as tellurium inclusions, and local variations in the electric field [7]. Thus, for large detection areas, a high degree of uniformity in the material properties is required before widespread use of CdZnTe detectors [8], [9] takes place. Detailed characterization of these detectors in terms of material and electrical properties are of utmost importance to achieve such high energy resolution below 1.0% at 662 keV and submillimeter position detection accuracy. However, detailed characterization of each detector module is not only time consuming but also requires a sophisticated experimental setup, multiple setups, and skilled manpower. On the other hand, deployment of such detector arrays requires precise characterization of the individual detectors and knowledge of the defects within the sensors spatially and temporally. Typically sensors with defects are discarded, which significantly reduces manufacturing yield, increases production cost and results in financial loss.

This work is licensed under a Creative Commons Attribution-NonCommercial-NoDerivatives 4.0 License.
For more information, see https://creativecommons.org/licenses/by-nc-nd/4.0/

In order to solve this important problem, we utilize a machine learning approach. Machine learning- and deep learning (DL)-based models have not only been popular in the last few years but also have created a paradigm shift in fields such as image processing, computational photography, natural language processing, and others. More recently, there has been a focus on applying machine learning to materials, drug discovery, physics-based systems and others. To the best of our knowledge, **this is the first contribution to characterization of radiation detectors using learning-based approaches.**

DL [10], a subarea of machine learning, has been a popular approach in the recent past, with convolutional neural networks (CNNs) [11]–[13], recurrent neural networks (RNNs) [14], [15] and generative adversarial networks (GANs) [16] being the most popular architectures. Work such as [17]–[19] has been done by one of the authors in the areas of DL. Typically, no physics knowledge is incorporated into the design of these models, but instead input–output data pairs are used to train the model. Depending on the size and capacity of the model, the data required to train it is typically very large. In many instances such as image processing and natural language processing, there are publicly available datasets which serve as training and testing data for the DL models. However, in the field of radiation detector characterization there is no such publicly available dataset (to the best of the authors' knowledge).

In this work, we propose a novel physics-inspired learning model derived from the physical charge transport equations for both electrons and holes in RTSD. The detector is spatially discretized into voxels. The physical charge transport equations are utilized to model each voxel. Compared to a conventional CNN or RNN model, which typically has millions of trainable parameters, our model has the same number of trainable parameters as the number of unknowns in the actual physical system. This results in the requirement for minimal amount of training data as this amount is proportional to the number of trainable weights. Conceptually, a lot of prior knowledge about the described physical process was used in designing the network, and therefore a smaller amount of information needs to be learned when a physics-agnostic network is used. Additionally, the learned weights are directly interpretable as representing meaningful detector material properties.

The proposed learning-based physical model aims to solve the following problems currently plaguing the characterization of radiation detectors with a reasonable detection area for wide scale implementation in medical imaging and security applications.

1) Fine characterization of detector material properties with spatial and temporal uniformity in a fast and efficient way.
2) Determination of detector material properties as per industry standards.
3) Micron-level defect identification and characterization.
4) Application of corrections to the detector at micron-level.

The main contributions of this article are:

1) Demonstration of learning-based physical model framework of RTSD at a microscopic scale.
2) Design and optimization of a weighted loss function for training the model.
3) Development of models with various voxel sizes (100, 200, and 400) with single and multiple electron–hole injections to the model.

The article is organized as follows. Section II describes the related work. Section III deals in detail with the classical approach for RTSD modeling. Section IV introduces the scalable to micron-size voxel-based learning model and the loss function for training the model. Section V highlights the experimental studies done while Sections VI and VII cover the discussions and conclusions, respectively.

II. Related Work

One of the biggest challenges for CdZnTe is their performance under high photon fluxes (10^6 mm^{-2} s^{-1}). The detector is more prone to polarization effects in which the electrical field is modified in the detector due to the build-up of trapped charge in the crystal [6]. Recently developed high flux capable CdZnTe [4] has been characterized in high-flux scenarios [20] and charge transport properties, using pulse shape analysis of measured signals. The thermal ionization energies of the electron and hole traps were measured using thermoelectric emission spectroscopy and thermally stimulated conductivity in [21]. In [22], trap identification and lifetime determination have been done using a microwave cavity perturbation method in detector grade CdZnTe and HgI_2. In [23], CdZnTe samples were radially irradiated by 5 MeV focused proton beam to create electron–hole pairs and fill traps. Trapped charges were released by thermal reemission. Electron and hole traps were distinguished by excitation near the vicinity of the appropriate electrode. Surface imperfections including mechanical damage or adsorbed chemical species, known to trap charges or increase leakage current have been characterized using pulsed laser microwave cavity perturbation method selectively at the surface and in the bulk region of CdZnTe RTSD [24]. In [25], deep trap levels in CdZnTe were characterized by simultaneous multiple peak analysis based on thermally stimulated current (TSC) measurements. In [26], nine defect levels and irradiation-induced variations of trap signatures for these levels were observed on CdZnTe:Al using TSC measurements. In [27], the average trapping and detrapping times for holes were derived using the average hole trapping time τ_{h} as measured in [28]–[32] using the statistical model of charge collection efficiency based on known electron average trapping time. Average hole detrapping time τ_{dh} is extracted by direct comparison between measured and simulated using only signals from holes measured by the cathode electrode [33]–[37]. Xu *et al.* [38] studied the influence of deposition methods and type of metal contacts on the defects (recombination/trapping) at the metal/semiconductor interface. In [39], the effects of deep-level defects on the carrier mobility in CZT crystals are studied. Zaman *et al.* [40] showed 13 different trap levels in Indium doped CZT crystal. Characterization of the uniformity of high flux CdZnTe has been done in [7]. Clearly, in the literature, the electron and hole trap properties measured using

classical approaches provide an average behavior over the material and require cumbersome multiple experiments and high technical skills.

Integrating physics-based Modeling with Machine Learning is being done in different fields in the last couple of years [41]. The overall objectives with such approaches are: 1) improve predictions beyond state-of-art physical models; 2) parameterization of model; 3) solving forward partial differential equations (PDE); 4) develop inverse models; and 5) discover governing equations, and others. These models are based on: 1) Physics-guided learning as expressed by appropriate loss functions, performing auxiliary tasks, physics-guided initialization; 2) Physics-guided design of network architecture; 3) residual modeling; and 4) hybrid physics-DL model. Neural network models have been successfully applied to solving problems in physics governed by PDEs [42]–[45]. Development and implementation of physics constrained network and related work have been done by one of the authors in Vija *et al.* [46], Ritt *et al.* [47], and Sanders and Vija [48].

Classical state-of-the-art approaches provide us with material properties in the bulk of the material over a coarse spatial length scale. The variations and fluctuations in the material properties which are typically in finer spatial length scales are not obtained using the classical approaches. Our approach follows the principle of physics-guided design architecture. In this work, we propose a learning-based framework from physical equations to provide the material properties of RTSD with microscopic resolution below 100 μm, which is the first such result to the best of our knowledge. We were inspired by a physics-based learning model in the realm of light transport using a scattering model [49]. However, it must be emphasized that the physics of charge transport in RTSD (electrons and holes) generated by high energy photons incident on the detector is more complex than light transport modeled by Hamilton and Mohseni [49].

III. Classical Approach for Detector Modeling

In solid-state detectors, electrons and holes transport properties play a significant role in selecting detectors for any application. Compensation techniques used to increase the resistivity of RTSD (mostly known to be plagued by shallow defect levels) introduce deep defect levels in the material [50]. The deeper defects act as longer trapping centers for charges, degrading the performance of these devices. The trapping, detrapping, and recombination are governed by Shockley-Read–Hall Theory [51], [52]. Rodrigues and He [53] worked on techniques to measure more detailed properties of these materials using the charge transport equations driven by the charge continuity equations with multiple electron and hole defect levels—trapping centers—coupled with Poisson's equation [54]–[59]. The macroscopic equations in [60] describe the various phenomena occurring in the material when photons, X-rays or energetic gamma rays interact with the material usually by Photoelectric, Compton or Pair-Production type of interaction, creating electron–hole pairs. Once the electron–hole pairs are created the following phenomena occur: 1) drift of charges (electrons and holes); 2) free charges getting trapped and detrapped in defect levels within the material; and 3) recombination of free charges, which is modeled as the capture of free electrons followed by the capture of free holes in the material [61].

Equation (1) shows the dynamic concentration of free electrons n_{e} in excess of equilibrium. There is an increase of electron concentration at a spatial region due to charge creation in the bulk, drift of charges to that region and detrapping from trapped levels. On the other hand, there is reduction of charges in the same region due to diffusion, trapping, and recombination of charges. The model considers that the charges trapped never saturate the trapping centers, since excess carrier concentrations are small compared to the number of available trapping and recombination centers and the simplified equations can be used Prettyman [54]. In (1), only one trapping level for electrons has been shown, while in principle there can be several trapping levels, often referred to as shallow and deep trapping defect levels, respectively

$$\frac{\partial n_{\mathrm{e}}}{\partial t} + \nabla \cdot (n_{\mathrm{e}} \mu_{\mathrm{e}} \nabla \phi) - \nabla \cdot (\mathrm{D_e} \nabla n_{\mathrm{e}}) = -\frac{n_{\mathrm{e}}}{\tau_{\mathrm{eT1}}} + \frac{\tilde{n}_{e1}}{\tau_{\mathrm{eD1}}} + \cdots + \delta_{\mathrm{e}} \quad (1)$$

where μ_{e} is the mobility of the electrons, ϕ is the voltage, $\mathrm{D_e}$ is the diffusion of electrons, $\tilde{n}_{e1}$, τ_{eT1}, and τ_{eD1} are, respectively, the concentration, trapping, and detrapping lifetime of electrons in trapped level 1, δ_{e} is the source term.

The increase in concentration of electrons in trapped level 1 is dependent on its own concentration $\tilde{n}_{e1}$, the amount of free electrons in excess of equilibrium n_e, trapping and detrapping lifetimes τ_{eT1} and τ_{eD1}, respectively, as shown in the following equation:

$$\frac{\partial \tilde{n}_{e1}}{\partial t} = \frac{n_{\mathrm{e}}}{\tau_{\mathrm{eT1}}} - \frac{\tilde{n}_{e1}}{\tau_{\mathrm{eD1}}}. \quad (2)$$

A similar equation applies to holes, as shown in (3) and (4) for holes with two trapping centers. Equation (4) shows the increase in holes trapped in trapping centers 1 and 2

$$\frac{\partial n_{\mathrm{h}}}{\partial t} + \nabla \cdot (n_{\mathrm{h}} \mu_{\mathrm{h}} \nabla \phi) - \nabla \cdot (\mathrm{D_h} \nabla n_{\mathrm{h}}) = -\frac{n_{\mathrm{h}}}{\tau_{\mathrm{hT1}}} - \frac{n_{\mathrm{h}}}{\tau_{\mathrm{hT2}}} + \frac{\tilde{n}_{h1}}{\tau_{\mathrm{hD1}}} + \frac{\tilde{n}_{h2}}{\tau_{\mathrm{hD2}}} + \cdots + \delta_{\mathrm{h}} \quad (3)$$

$$\frac{\partial \tilde{n}_{h1}}{\partial t} = \frac{n_{\mathrm{h}}}{\tau_{\mathrm{hT1}}} - \frac{\tilde{n}_{h1}}{\tau_{\mathrm{hD1}}}$$

$$\frac{\partial \tilde{n}_{h2}}{\partial t} = \frac{n_{\mathrm{h}}}{\tau_{\mathrm{hT2}}} - \frac{\tilde{n}_{h2}}{\tau_{\mathrm{hD2}}} \quad (4)$$

where n_{h} is the dynamic concentration of free holes in excess of equilibrium. μ_{h} is the mobility of the holes, $\mathrm{D_h}$ is the diffusion of holes. $\tilde{n}_{h1}$, τ_{hT1}, and τ_{hD1} are, respectively, the concentration, trapping, and detrapping lifetime of holes in trapped level 1. Similarly, $\tilde{n}_{h2}$, τ_{hT2}, and τ_{hD2} are, respectively, the concentration, trapping, and detrapping lifetime of holes in trapped level 2. δ_{h} is the source term.

The diffusion of the charges $\mathrm{D_{e,h}}$ for electrons e and holes h, is governed by mobility of electrons and holes μ_{e} and μ_{h}, respectively, along with the temperature of the material T and

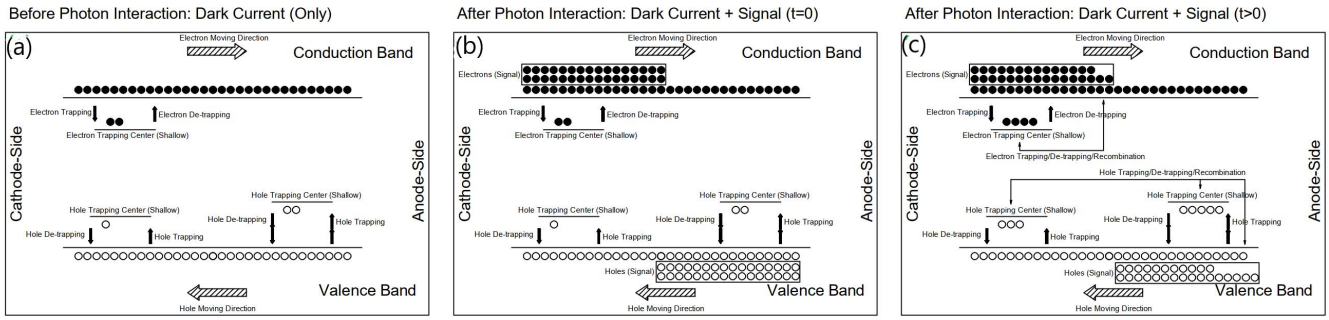

Fig. 1. (a) Energy level diagram of a RTSD showing one electron and two hole trapping centers, before photon interaction. (b) Electrons–holes in excess of equilibrium generated at $t = 0$. (c) Transport of electrons and holes by operating electric field along with trapping, detrapping, and recombination for $t > 0$.

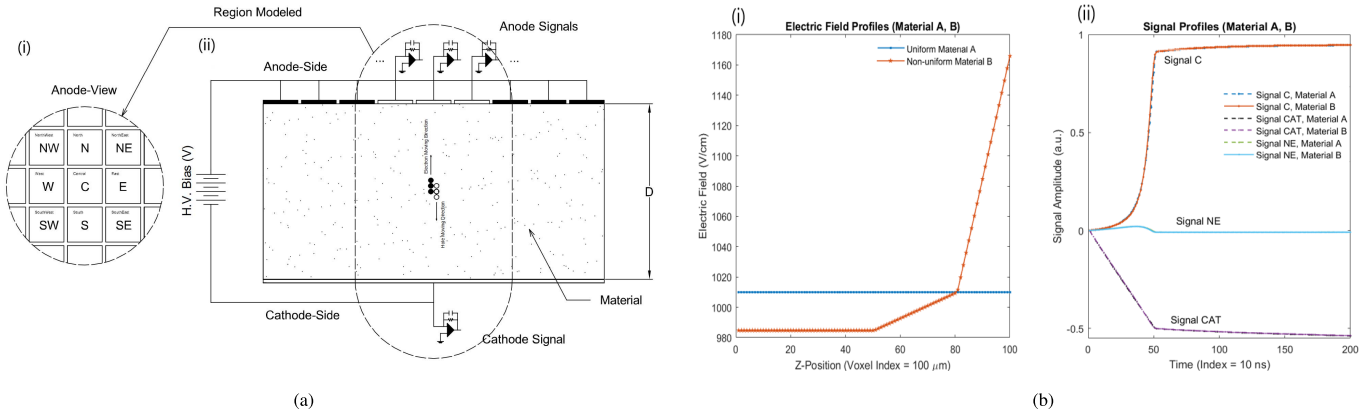

Fig. 2. (a): (i) Sensor pixelated anode pattern and (ii) Central region model illustrating pixelated anode design with uniform material and electrons–holes drift in bulk. (b): (i) Electric field profiles for simulated materials A and B and (ii) Anode Signals C, CAT and NE simulated for materials A and B (for electron–hole charge injected at Voxel 50). (a) Detector configuration. (b) Electric field and signal profiles.

Boltzmann's constant k as shown in the following equation:

$$\mathrm{D_{e,h}} = \mu_{\mathrm{e,h}} \frac{kT}{E,\, H}. \tag{5}$$

In (5), the subscripts e, h in the diffusion $\mathrm{D_{e,h}}$ and mobility $\mu_{\mathrm{e,h}}$ refers to the corresponding diffusion and mobility for electrons and holes, respectively. The denominator in (5), E, H refers to the electric charge of electrons and holes, respectively.

The drift of charges is dependent on the electric field E, which is shown in (6), with the voltage satisfying the Poisson equation as follows:

$$E = -\nabla\phi \tag{6}$$

$$\nabla^2\phi = -k\frac{q}{\epsilon}(n_{\mathrm{e}} + \tilde{n}_{e1} + n_{\mathrm{h}} + \tilde{n}_{h1} + \cdots). \tag{7}$$

Here, ϵ represents the permittivity of the RTSD material. Fig. 1 shows the energy band diagram of an RTSD for one electron and two hole trapping centers before and after a high-energy photon interaction occurs within the detector. Signals collected at the electrodes arise due to the movement of charges [62]–[66]. The detector setup is shown in Fig. 2(a)(i, ii) with the nine grid electrodes on the anode side [north west (NW), N, north east (NE), W, C, E, south west (SW), S, and South East (SE)] and one single large cathode electrode (CAT). Fig. 2(b)(i) shows two cases of the electric field—uniform and piecewise linear which are plausible cases encountered in the detector, while Fig. 2(b)(ii) shows the signals observed in the cathode electrode and three adjacent anodes (center or collecting anode, north, and NE or neighbors) for electron–hole pair injection at voxel position 50, where, in this case, the cathode was at position 0 and the anode at position 100. The plots shown in Fig. 2(b) are simulated data in MATLAB. At a quick glance, there is almost no difference in the signals generated at the electrodes due to the two electric fields, A and B as shown in Fig. 2(b)(ii). However, with a close look at the electric field profiles in Fig. 2(b)(i), we can see distinct differences between them. Our learning-based approach can clearly distinguish between these two electric field profiles as shown in Fig. 2(b)(i) from the signals shown in Fig. 2(b)(ii), along with the charges, despite not being visually observable in the signals at the electrodes.

The data for training the proposed learning model has been generated using the classical equations, (1)–(7). A MATLAB code has been developed to define the charge transport equations in the detector, by defining the trapping, detrapping and recombination lifetimes of electrons and holes as constant predefined parameters, with varying the electric field along the material. This classical model has been created by spatially discretizing the detector. For a charge input at different voxels in this classical model, the signals are generated in the cathode and pixelated anode. Additionally, the free and trapped charges in different spatial pixel locations are computed. The signals and free and trapped charges are computed for each time step, with the total number of time steps defined *a priori*.

The input–output data for training the learning-based model consists of the input electron–hole pair injected in the material at a known voxel position along with the signals, free and trapped charges in different spatial voxels of the classical model over different time steps in the simulation.

IV. Learning-Based Approach for Detector Modeling

A learning-based model has been developed from (1)–(7) for the detector material. As highlighted in Section III, this is the first approach in the literature taken to model a room temperature semiconductor detector with learning-based principles using the physical equations. The current state-of-art techniques only find out the bulk average properties of the detectors which can be spatially determined with finer resolution (microscopic sizes) in our novel approach.

A. Voxel Based Learning Model

In this work, we introduce a novel method to determine the material properties such as $\mu_{\mathrm{e,h}}$, τ_{eT1}, τ_{eD1}, τ_{hT1}, τ_{hD1} and recombination coefficients of free and trapped electrons and holes at spatially discretized locations in the detector material. In order to do so, we subdivide the detector material into N voxels, with N being the number of subdivisions in the material in any dimension 1-D, 2-D, or 3-D. In each of the discretized volumes (termed as voxels) of the material, material properties such as $\mu_{\mathrm{e,h}}$, $\tau_{\mathrm{eT1},i}$, $\tau_{\mathrm{eD1},i}$, $\tau_{\mathrm{hT1},i}$, $\tau_{\mathrm{hD1},i}$ are defined. We refer to these discretized properties as weights spatially distributed inside the material. For instance, the mobility μ_{e} is converted into N discrete values of $w_{Trpt,e}$ in the material. Now, the relation between μ_{e} and μ_h can be separately modeled as unknown parameters. The relation between the mobility of electrons μ_{e} and holes μ_{h}, $(\mu_{\mathrm{h}} = 0.1\mu_{\mathrm{e}})$, is considered in the formulation. It must be emphasized here that this relation is not always true. However, in this work, for simplicity, this relation has been used. Similarly for other material properties, N parameters of each of the properties are being used in the model. This model, therefore, allows the determination of the unknown parameters of the material with higher precision. For each of these coefficients (referred here as τ in general), we compute the number of charge particles (electrons or holes) remaining in that particular level as $N_{\mathrm{left}} = N_0 e^{-t/\tau}$, where N_0 and N_{left} are the number of charged particles at a particular level at $t = 0$ and at time t, respectively. Thus, given the time $t = t_1$, (example, $t_1 = 10$ ns for the 100 voxel model) and given τ, we can compute the fraction of charges transitioning from an energy level to another. We use these charges in our model. For a particular material property τ, we can find out the fraction of charges remaining in that energy level.

A voxelized representation of the detector in one dimension is shown in Fig. 3. Linearly the material is divided into N voxel segments with the electrodes at either end, anode on the right, and cathode on the left. In this work, we consider an anode grid with nine electrodes as shown in Fig. 2(a) [1]. However, in general, we can consider the electrodes (cathode/anode) of any structure or configuration. With respect to the detector, the high-energy radiation (for example Gamma rays or X-rays) can interact in any position of the detector.

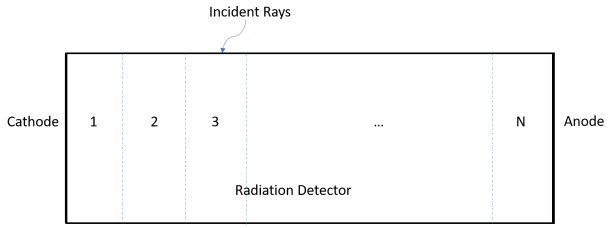

Fig. 3. Voxel discretization with electrodes at the ends.

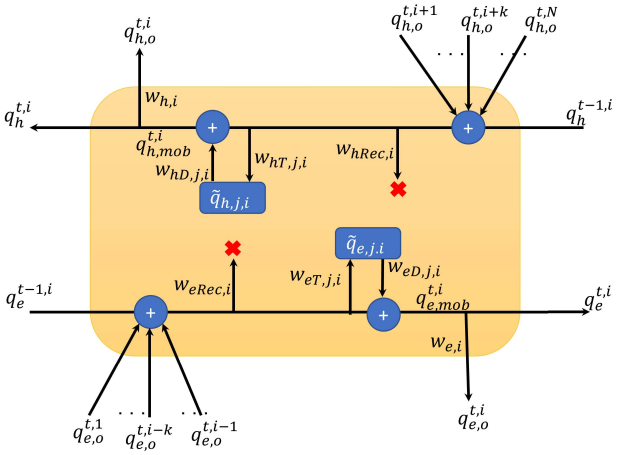

Fig. 4. Operations in voxel i at time t.

The resultant physical model in turn is a discretized version of the physical phenomena occurring in each voxel of the detector over time. Thus, the model can be thought of as being analogous to a network composed of long short term memory (LSTM) or gated recurrent unit (GRU) cells [67]. However, the weights in an LSTM/GRU block [67] can be tuned to the physical phenomena occurring inside the voxel of the material. Typically, such a model would require more weights. This will lead to not only training the model with more weights but also requiring more training data and time. In order to remove these limitations, we propose a model which corresponds to the exact physics-based equations at time t for voxel i in Fig. 4.

In Fig. 4, the operations taking place in voxel i at time t are shown in detail. At any time $t-1$, the charge in voxel i in free state is $q_h^{t-1,i}$ for holes and $q_e^{t-1,i}$ for electrons. Under the influence of Electric Field, holes drift at time t from other voxels $i+1, \ldots, i+k, \ldots, N$, to voxel i, with charges $q_{h,o}^{t,i+1}, \ldots, q_{h,o}^{t,i+k}, \ldots, q_{h,o}^{t,N}$, respectively. These charges are added into the existing charge $q_h^{t-1,i}$ to form the total charge due to holes in voxel i at time t, referred here as $q_{h,\mathrm{int}}^{t,i}$. The subscript int refer to the total or integrated charge due to sum of all holes in voxel i at time t. Some of the holes recombine with the intrinsic electron concentration in the bulk of the material with weight $w_{h\mathrm{Rec},i}$, which in voxel i at time t is referred as $q_{h,\mathrm{Rec}}^{t,i}$. The subscript Rec refers to recombination. The presence of trapped hole centers in the

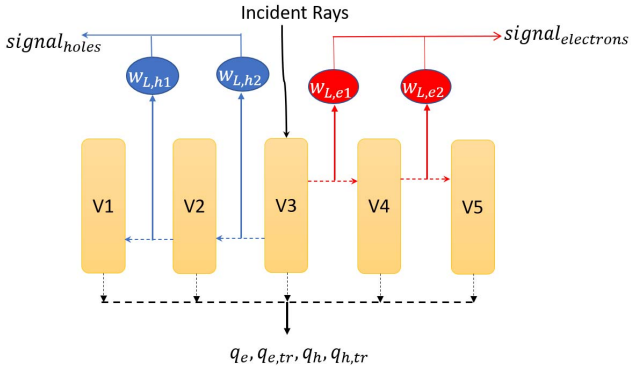

Fig. 5. Computations in a sample configuration with five voxels in 1-D.

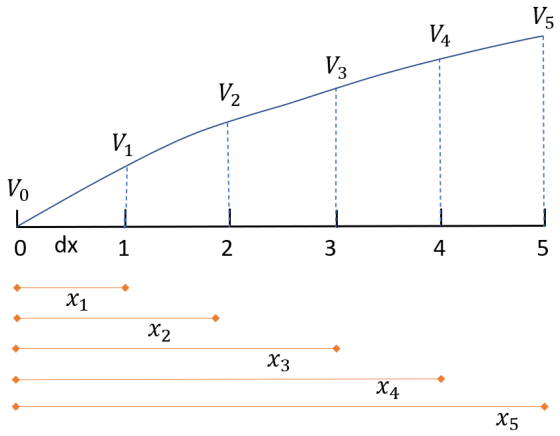

Fig. 6. Voltage relation between voxels.

material traps some of the holes and detraps holes back as excess hole concentration over bulk, as indicated, respectively, by the trapping and detrapping weights $w_{\mathrm{hT},j,i}$ and $w_{\mathrm{hD},j,i}$, for hole trapping level j in voxel i. The total holes which are available for transport in the valence band of voxel i at time t is termed as mobile or free holes, $q^{t,i}_{h,\mathrm{mob}}$, and mob in the subscript denotes the mobile holes. In Fig. 4, we show just one level of trapping centers (for both electrons and holes). However, in principle, depending on the material properties there can be several trapping centers for both electrons and holes. A fraction of holes ($w_{h,i}$) drift out of voxel i as ($q^{t,i}_{h,o}$), while the remaining holes are left behind in voxel i as ($q^{t,i}_{\mathrm{h}}$) at time t. Same operations are repeated for electrons, as shown in the bottom half of Fig. 4. The stepwise computations for holes in voxel i are shown in the following equations:

$$q^{t,i}_{h,\mathrm{int}} = q^{t-1,i}_{\mathrm{h}} + \left(q^{t,i+1}_{h,o} + \cdots + q^{t,i+k}_{h,o} + \cdots + q^{t,N}_{h,o}\right) \tag{8}$$

$$q^{t,i}_{h,\mathrm{Rec}} = w_{h\mathrm{Rec},i} \times q^{t,i}_{h,\mathrm{int}} \tag{9}$$

$$q^{t,i}_{h,\mathrm{mob}} = q^{t,i}_{h,\mathrm{int}} \times \left(1 - w_{h\mathrm{Rec},i} - w_{\mathrm{hT},j,i}\right) + \left(\tilde{q}_{h,j,i} \times w_{\mathrm{hD},j,i}\right) \tag{10}$$

$$q^{t,i}_{h,o} = w_{h,i} \times q^{t,i}_{h,\mathrm{mob}}. \tag{11}$$

Fig. 5 shows the model with the detector discretized into 5 voxels (for explanation purposes only). The high energy rays are incident on Voxel $V3$ creating electron–hole pairs in that voxel. The electrons drift toward the anode (right of Voxel $V5$), while the holes drift toward the cathode (left of Voxel $V1$). While drifting from one voxel to another, the electron charges are multiplied by difference of potentials, shown as $w_{L,e1}$ and $w_{L,e2}$ for electrons drifting between voxel $V3$ and $V4$, and $V4$ and $V5$, respectively, to generate electrical signals for electrons ($\mathrm{signal}_{\mathrm{electrons}}$). Similar phenomena occur to generate electrical signals for holes ($\mathrm{signal}_{\mathrm{holes}}$). The electrons and holes induce the signal at the anode and cathode, calculated as per the Schockley–Ramo Theorem [63]. In each of the voxels $V1 - V5$, the free charges and the ones trapped in the trapping centers (electrons and holes), as well as the signals generated at the electrodes are recorded.

B. Voltage Relation Between Voxels

In the formulation of the model, we consider the voltages at the electrodes at the ends of the detector to be fixed V_i and V_f. In general, the voltage can vary in any manner within the RTSD. However, in this article, we consider the voltage at each voxel of the detector to increase linearly stepwise from the previous one, as shown in Fig. 6. The voltage increases from the cathode to the anode. We consider Voxel 0 with reference position x_0, and successive Voxels $1, 2, \ldots, 5$, (denoted by $V_1, V_2, \ldots, V_5$) at positions $x_1, x_2, \ldots, x_5$ with each successive voxel at distance dx, (for example, $x_5 - x_4 = x_4 - x_3 = dx$) from the previous voxel. In between the two voxels (for example voxels 3 and 4), we can apply (12), where voltages V_3 and V_4 are linearly related. Similarly for voxels 4 and 5, we can apply (13), where Voltage V'_4 and V'_5 are linearly related. In these equations, C_{31}, C_{32}, C_{41} and C_{42} are learnable coefficients. Now, the voltage V_4 and V'_4 from (12)(b) and (13)(a) must match. Thus combining we can formulate an error term, $\mathrm{error}_{\mathrm{voltage}}$ as the difference between V_4 and V'_4 normalized over the distance of Voxel 4 from origin 0, x_4, defined in the following equation:

$$V_3 = C_{31}x_3 + C_{32} \tag{12a}$$

$$V_4 = C_{31}x_4 + C_{32} \tag{12b}$$

$$V'_4 = C_{41}x_4 + C_{42} \tag{13a}$$

$$V'_5 = C_{41}x_5 + C_{42} \tag{13b}$$

$$\mathrm{error}_{\mathrm{voltage}} = (C_{31} - C_{41}) - \frac{(C_{42} - C_{32})}{4dx}. \tag{14}$$

C. Loss Function

The model is trained with input–output pairs of data. The input data are the position of injected electron–hole pair and the output data are the signals obtained at the electrodes along with the electrons and holes (free and trapped) in each of the voxels over time. During training of the model, the loss function is computed as the sum of the squared errors between the signals at the electrodes and charges in the voxels compared to the ground truth signals along with the $\mathrm{error}^2_{\mathrm{voltage}}$. The overall loss function for this model is shown in (15). The loss function in (15) is shown for one trapping center for both electrons and holes for illustration. However, we perform simulation experiments considering CZT detector

with two trapping centers for holes and 1 trapping center for electrons [21], [60]. We generate the learning-based model for CZT detector which is popularly used in radiation imaging systems. However, in general, there can be several trapping centers for both electrons and holes, and thus several such terms, whose number is predefined, and the learning-based model has to be designed accordingly. In the loss function, the errors due to the signals and voltage are grouped together, free and trapped electron charges are grouped together, and free and trapped charges due to holes are grouped together with weighting terms k, l, and n, respectively. Clearly, as k, l, and/or n are varied, the errors due to those terms vary. The higher the value of the parameters, the lower the errors associated with those terms. In these error terms, the subscript gt for a particular parameter X (for instance, X is signal or q_e) refers to the ground truth data for that parameter X generated in MATLAB using the classical model as described in Section III and the subscript L for the same parameter X refers to the data generated by the learning-based model

$$\begin{aligned}\text{LF} &= k\Big[\left(\text{signal}_{\text{gt}}-\text{signal}_L\right)^2+\text{error}^2_{\text{voltage}}\Big]+l\Big[\left(q_{e,\text{gt}}-q_{e,L}\right)^2 \\ &\quad+\left(q_{et,\text{gt}}-q_{et,L}\right)^2\Big]+n\Big[\left(q_{h,\text{gt}}-q_{h,L}\right)^2+\left(q_{ht,\text{gt}}-q_{ht,L}\right)^2\Big]. \end{aligned} \tag{15}$$

D. Implementation Details

In this learning-based voxelized physical model, the input to the model is the injection positions of the electron–hole pairs generated due to the interaction of the high energy rays with the RTSD along with the magnitude of the injected charges. The magnitude of the injected charges is normalized to 1. The output of the model is the signals from the electrodes, free and trapped electron, and hole charges in the voxels over time. The model weights as described in Section IV-A are initialized to an initial value. Based on the electron–hole pair input to this model, the output (signals, free, and trapped charges) is computed over time. The model consists of training and testing phases. In the training phase, the loss is computed using (15) for every electron–hole input pair based on the outputs from this model and the ground truth output data over time. Since our model is a recurrent network structure over time, backpropagation through time (BPTT) [68], [69] is used to compute the gradients of the loss with respect to the trainable (or tunable) weights of the model. BPTT unfolds the learnable model in time by creating several copies of the model which can be treated as a feed forward deep network with tied weights. The update of the trainable weights is based on a stochastic gradient descent method—ADAM optimization [70], which is based on adaptive estimation of first-order and second-order moments. ADAM optimizer is used with a learning rate of 5×10^{-4} with two momentum terms set as $\beta_1 = 0.9$ and $\beta_2 = 0.999$. Learning rate higher than 5×10^{-4} causes oscillations in the loss function, while a lower learning rate slows down convergence. In each epoch (iteration), the ADAM optimization updates the trainable weights of the model based on the gradients, with the goal to minimize the loss function over the epochs. This learning-based physical model is developed using Tensorflow library [71] in Python in eager execution mode. Tensorflow's eager execution mode provides a flexible machine learning platform using Python control flow which helps in easier debugging and provides an intuitive interface. Over the epochs, the weights of the model such as electron transport weights $w_{\text{Trpt},e,i}$, electron trapping weights $w_{\text{eT},i}$, electron detrapping weights $w_{\text{eD},i}$, and other weights in voxel i as shown in Fig. 4 in the learning-model are trained. The weights in these voxels are trained simultaneously over epochs. Once the model is trained, the model can be tested based on the electron–hole pair input at the voxel position. The injection position is different from the ones used for training the model. In the testing phase, there is no computation of loss. Only the signals and charges are obtained in each time step as output from the model.

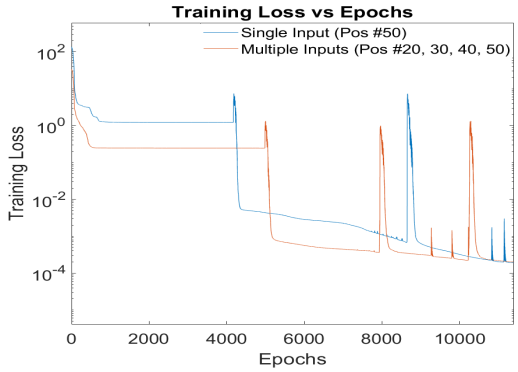

Fig. 7. Training loss for single and multiple inputs (for $k = l = n = 1$) in (15).

V. Experimental Studies

In order to train and test the model actual measured data would be needed. Unfortunately, no such dataset is available in the literature for RTSD. We generate synthetic data using the classical model developed in MATLAB using (1)–(7), as described in Section III. The experimental training data consist of electron–hole pairs injected at different voxels and the corresponding signals in the electrodes over time along with the electron and hole distributed charges (free and trapped) in the voxels over time. Since the learning-based model is developed in a voxelized manner, the training data generated using the classical approach is also voxelized. The experimental data using the classical model has been developed for different conditions such as voxel sizes, time steps, and other conditions. During the training process, the loss is monitored over epochs and allowed to converge to less than 0.005 or until it stops decreasing. In our experiments, there is no significant improvement in the model coefficients/weights below this threshold loss value.

A. Experimental Studies With Unweighted Loss Function

We performed experimental studies with $k = l = n = 1$ in (15) and a model with 100 voxels. The voxel at one end,

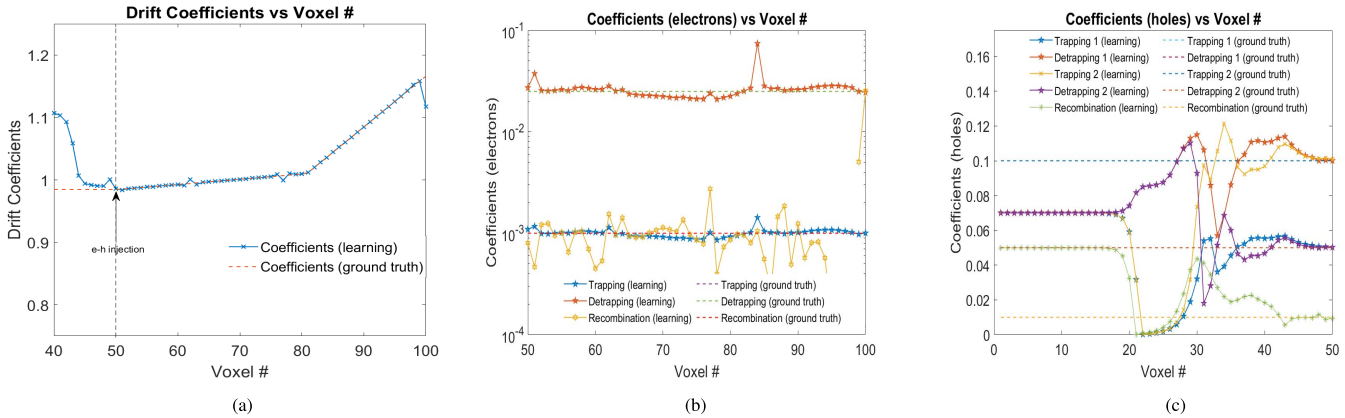

Fig. 8. (a) Drift coefficients (μ_e), (b) electron coefficients ($w_{\text{eT},1}$, $w_{\text{eD},1}$, $w_{e\text{Rec}}$), and (c) hole coefficients ($w_{\text{hT},1}$, $w_{\text{hD},1}$, $w_{\text{hT},2}$, $w_{\text{hD},2}$, $w_{h\text{Rec}}$) for e–h injection at voxel 50. (a) Drift coefficients. (b) Electron coefficients. (c) Hole coefficients.

voxel 100 is connected to the anode terminal while the voxel at the other end, voxel 0 is connected to the cathode terminal. The experimental data used for learning the model consists of electrons and holes transport, one trapping center for electrons and two trapping centers for holes along with recombination of electrons and holes in the detector. This is based on the properties of the CZT detector as described in [60]. The phenomenon of diffusion is ignored in the experiments, as it has negligible contribution to the overall signal and charge output in our proposed application, which is aimed at keV energy range, high electric field, and mm-size anode pixels. In general, diffusion can be included in the model depending on whether it has a significant contribution to the overall charge transport and signal at the electrodes. The material is considered as 1D and discretized into 100 equal partitions, termed as voxels for generalization, and the experiments are done with timesteps of 10 ns resolution. The simulated detector has a size of 10 mm, with a total simulation time of 2 μs. The training losses over epochs for single and multiple inputs are shown in Fig. 7. The training loss decreases consistently over the epochs. There are increases in training loss at certain epochs which later reduces, while the gradient descent optimizer (ADAM) tries to find a stationary point. However, the overall loss function reduces over the epochs.

1) Experiment With Charge (e–h) Injection at a Particular Position: Unit charge in terms of electron–hole pair was injected at voxel position 50, which is at the middle of the material. The learned weights of the trained model represent the properties of the detector material. Fig. 8(a)–(c) show the drift coefficients, electron coefficients, and hole coefficients, respectively. The drift coefficients follow the ground truth which is piecewise linear in the material. The drift coefficients to the right of the point of charge injection are trained due to the movement of electrons while the drift coefficients to the left of the injection point are trained due to the movement of holes. In Fig. 8(a), the drift coefficients shown are due to the drift of electrons. For the holes, the drift coefficients were one-tenth of that shown in Fig. 8(a) due to lower mobility of holes compared to electrons, which is known *a priori* in the model. In Fig. 8(b), the electron coefficients consist of the electrons trapped and detrapped in the trapping center along with the recombination of electrons in the bulk of the material. The trapping and detrapping coefficients follow the ground truth for most of the voxels in the material, while the recombination coefficient is oscillating near the end of the material (higher voxels). This is primarily due to the lower value of the gradients for the recombination coefficients of electrons at higher voxels. For the hole coefficients in Fig. 8(c), holes travel only a couple of voxels toward voxel 0 from the point of injection, and hence, coefficients in voxels around 40 to 50 only were trained in the model.

2) Experiment With Charge (e–h) Injection at Multiple Positions: Unit charge in terms of an electron–hole pair is injected at voxel positions 20, 30, 40, and 50. Fig. 9(a)–(c) shows the drift coefficients, electron coefficients, and hole coefficients, respectively. The gradients in the ADAM optimization are computed for the loss in (15) for electron–hole pair injection at a single voxel, and the overall gradient update is performed based on the sum of these individual gradients. The drift coefficients follow the ground truth closely as shown in Fig. 9(a). It is seen in Fig. 9(c) that hole coefficients (for trapping centers 1 and 2 and recombination coefficients) also follow closely the ground truth coefficients. There are slight oscillations near the injection points of the electron-hole pair, which are mostly due to the learning of the hole coefficients for voxels less than ten voxels away which is the length of the injection intervals of the e–h pairs. Clearly, the closer the injection points, the lower the oscillations in the hole coefficients. However, it is seen that the electron coefficients [Fig. 9(b)] oscillate around the ground truth values for the recombination coefficients. We explore different combinations of k, l, n values in Section V-B and show better convergence of the values of the electron recombination and other coefficients.

B. Experimental Studies With Weighted Loss Function

We performed experimental studies with k, l, $n \in \{0.1, 1.0, 10.0, 100.0\}$ in (15) using the 100 voxel size model. Now k, l, n can take any finite values. However, in the experimental studies, k, l, and n are chosen to be linear in logarithmic scale from 0.1 to 100, which spans a wide range.

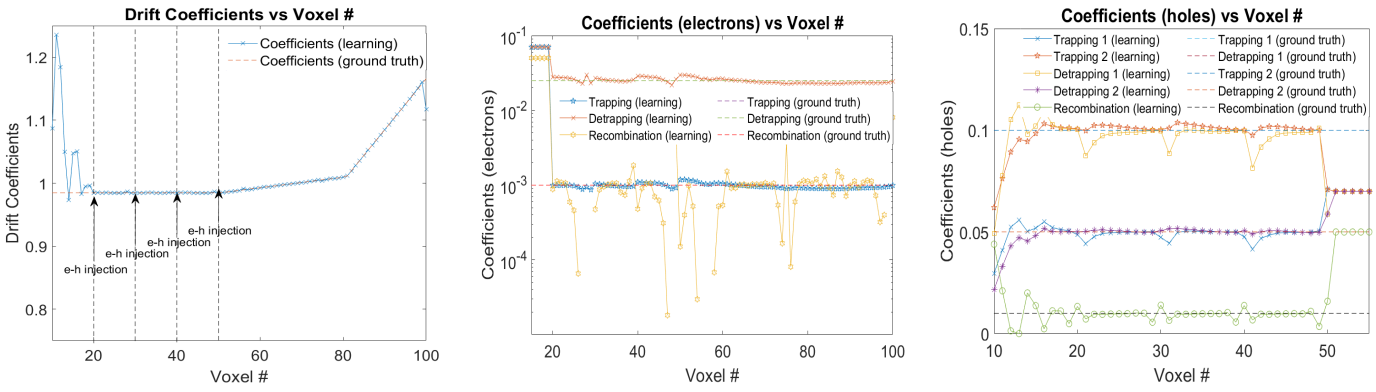

(a) (b) (c)

Fig. 9. (a) Drift coefficients (μ_e), (b) electron coefficients ($w_{\text{eT},1}$, $w_{\text{eD},1}$, $w_{e\text{Rec}}$), and (c) hole coefficients ($w_{\text{hT},1}$, $w_{\text{hD},1}$, $w_{\text{hT},2}$, $w_{\text{hD},2}$, $w_{h\text{Rec}}$) for e–h injection at voxels 20, 30, 40, and 50. (a) Drift coefficients. (b) Electron coefficients. (c) Hole coefficients.

TABLE I
TOP FIVE MINIMUM NMSE VALUES FOR VARYING k, l, n

	k, l, n	NMSE
1	$0.1, 100, 100$	0.1761
2	$0.1, 100, 10$	0.1926
3	$1, 100, 100$	0.2537
4	$0.1, 100, 1$	0.4102
5	$0.1, 10, 1$	0.4617

The experimental data and the model size used for learning the model are the same as in Section V-A, consisting of transport, trapping, and detrapping centers for electrons and holes, along with a recombination of charges.

1) Experiment With Charge (e–h) Injection at a Particular Position: A unit charge in terms of an electron–hole pair was injected at voxel position 50, at the center of the detector. For the combinations of k, l, and n, we obtain 64 sets of trained parameters for the model. For each of these 64 sets, we computed the normalized mean squared error (NMSE) between the actual coefficients used in the classical model and the learned weights in the model, referred to as NMSE in (16). NMSE is used for computing the error as the learned coefficients have values at different scales. Normalizing the mean squared errors removes this scaling effect. In (16), $w_{\text{Trpt},e,\text{lr}}$ and $w_{\text{Trpt},e,\text{gt}}$ refer to the learned and ground truth drift/transport coefficient for electrons, respectively. Similarly, other weights refer to electron and hole trapping, detrapping, and recombination weights. The weights are analogous to the trapping, detrapping, and recombination lifetime in the actual detector. The top 5 smallest NMSE values are shown in Table I. For injection at voxel 50, the NMSE error was computed for voxels 50 to 100 for drift/transport coefficients, voxels 50 to 100 for NMSE due to electron weights, and voxels 37 to 50 for NMSE due to hole weights. The range of voxels used for hole computation was selected based on the mobility of holes and calculated drift. For electrons, voxel 100 refer to the end of the material and for holes, voxel 37 refers to the maximum drift of holes. Generally speaking, the maximum drift locations from the injection point of the charges must be

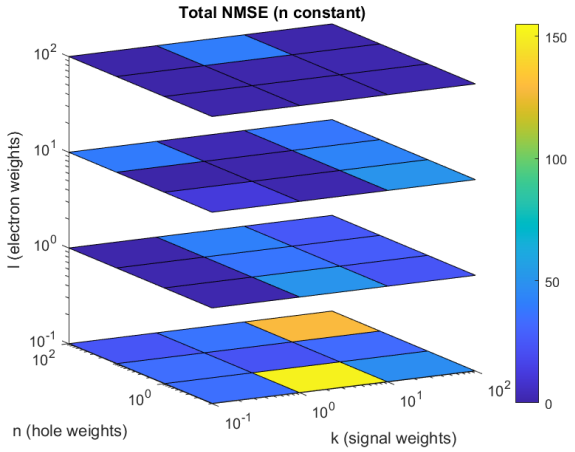

Fig. 10. NMSE values for varying k, l, n values.

used for computing the NMSE

$$\begin{aligned}\text{NMSE} = &\left\{\frac{w_{\text{Trpt},e,\text{lr}} - w_{\text{Trpt},e,\text{gt}}}{w_{\text{Trpt},e,\text{gt}}}\right\}^2 + \left\{\frac{w_{\text{eT,lr}} - w_{\text{eT,gt}}}{w_{\text{eT,gt}}}\right\}^2 \\ &+ \left\{\frac{w_{\text{eD,lr}} - w_{\text{eD,gt}}}{w_{\text{eD,gt}}}\right\}^2 + \left\{\frac{w_{\text{hT1,lr}} - w_{\text{hT1,gt}}}{w_{\text{hT1,gt}}}\right\}^2 \\ &+ \left\{\frac{w_{\text{hD1,lr}} - w_{\text{hD1,gt}}}{w_{\text{hD1,gt}}}\right\}^2 + \left\{\frac{w_{\text{hT2,lr}} - w_{\text{hT2,gt}}}{w_{\text{hT2,gt}}}\right\}^2 \\ &+ \left\{\frac{w_{\text{hD2,lr}} - w_{\text{hD2,gt}}}{w_{\text{hD2,gt}}}\right\}^2 \\ &+ \left\{\frac{w_{\text{hR,lr}} - w_{\text{hR,gt}}}{w_{\text{hR,gt}}}\right\}^2 + \left\{\frac{w_{e\text{R,lr}} - w_{e\text{R,gt}}}{w_{e\text{R,gt}}}\right\}^2. \quad (16)\end{aligned}$$

Clearly, for $k = 0.1$, $l = 100$ and $n = 100$, the NMSE is minimum with calculated value of 0.1761. The plot of the different NMSE values for varying k, l, n is shown in Fig. 10. The lower NMSE is favored for lower k and higher l, n values. Fig. 11 shows the drift coefficients (a), detrapping two level for holes (b), and electron recombination weights (c) for different l and n values for $k = 0.1$. It can be seen that for $k = 0.1$, $l = 100$, $n = 100$, the learned coefficients are closest to the

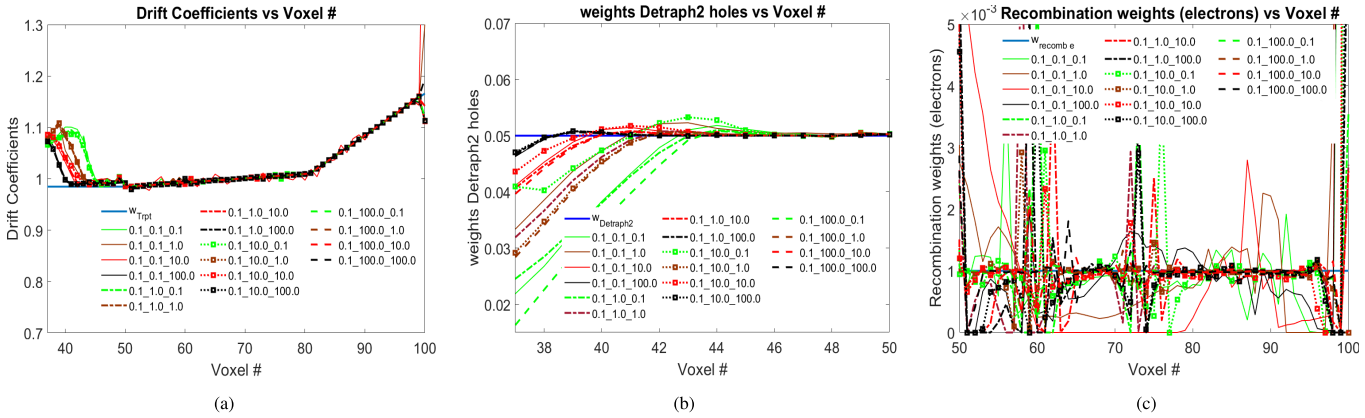

(a) (b) (c)

Fig. 11. (a) Drift coefficients (μ_e), (b) detrapping two hole coefficients ($w_{\mathrm{hD},2}$), and (c) recombination electron coefficients ($w_{e\mathrm{Rec}}$) for e–h injection at Voxel 50 for $k = 0.1$ and varying l, n. Plot legend refers to k_l_n values. Readers are suggested to enlarge the figure for closer view. (a) Drift coefficients. (b) Detrapping two level holes. (c) Recombination electron.

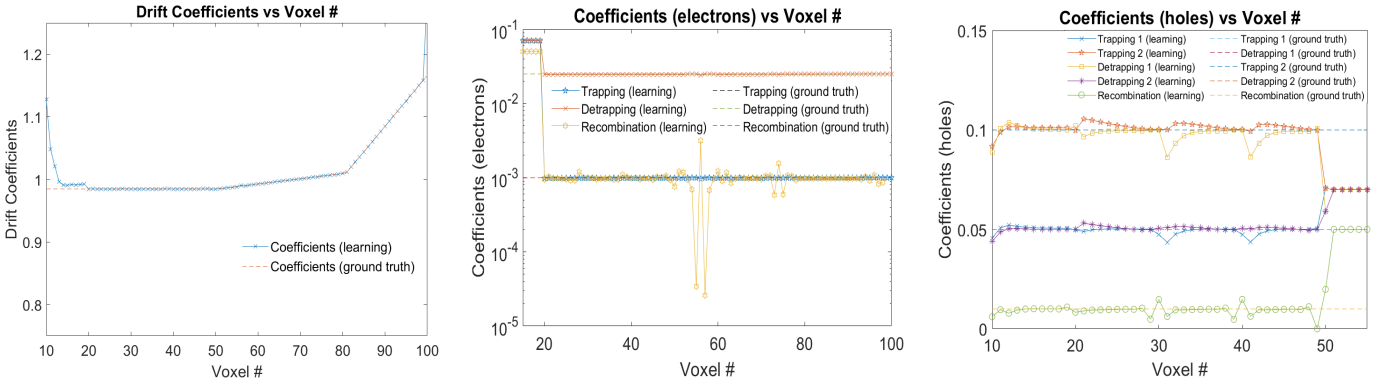

(a) (b) (c)

Fig. 12. (a) Drift coefficients (μ_e), (b) electron coefficients ($w_{\mathrm{eT},1}$, $w_{\mathrm{eD},1}$, $w_{e\mathrm{Rec}}$), and (c) hole coefficients ($w_{\mathrm{hT},1}$, $w_{\mathrm{hD},1}$, $w_{\mathrm{hT},2}$, $w_{\mathrm{hD},2}$, $w_{h\mathrm{Rec}}$) for e–h injection at voxels 20, 30, 40, and 50 with $k = 0.1$, $l = 100$, $n = 100$. (a) Drift coefficients. (b) Electron coefficients. (c) Hole coefficients.

coefficients used in the classical model to generate training data.

2) Experiment With Charge (e–h) Injection at Multiple Positions: It was shown in Section V-B.1 that the calculated NMSE was optimized for $k = 0.1$, $l = 100$, and $n = 100$. We use this combination of k, l, n values in the learning model for injecting charges at multiple voxel positions of 20, 30, 40, and 50. Fig. 12(a)–(c) shows the drift, electron, and hole coefficients, respectively, for material B (material B has nonuniform electric field profile as shown in Fig. 2(b) [1]). It is observed that for the optimal regularized parameters k, l, n, the learned model coefficients fit the ground truth coefficients more closely compared to the learned model coefficients with equal regularization parameters as shown in Fig. 9. The weighted model clearly prioritizes signals at the electrodes, charges (free and trapped) due to electrons and holes differently than the unweighted model. Now, since these hole and electron charges are more fundamental and the signals are generated only due to charge motion, the higher weightage of charges (free and trapped) in the loss function compared to the signals drives the model to its optimized material parameters better than the unweighted model. In both cases, e–h injection is at exactly the same voxel locations of 20, 30, 40, and 50. Clearly, choosing appropriately the regularization parameters in the loss function improved the accuracy in the learned parameters. We also show similar results and conclusions for the electron, hole, and recombination coefficients in Fig. 13(a)–(c), respectively, for material A with electron–hole pairs fed in position 9, 19, 29, 39, 49, 59, 69, 79, 89, and 99 in a 100 voxel model (material A has uniform electric field profile as shown in Fig. 2(b) [1]). There is some oscillatory behavior in the hole trapping, detrapping, and recombination coefficients as the holes do not travel large distances from their point of injection.

C. Model With Different Voxel Sizes

The model can be designed with larger than 100 number of voxels. In this article, we also show the results of the model with 200 and 400 voxels. For material with the same dimension as before, increasing the number of voxels in the model will reduce the size of each voxel. The decrease in voxel size in the model will improve the response characteristics of the output signals. In Sections V-C1 and V-C2, we show the performance of the model with a higher number of voxels having charge (e–h) injection at both a single position and multiple positions.

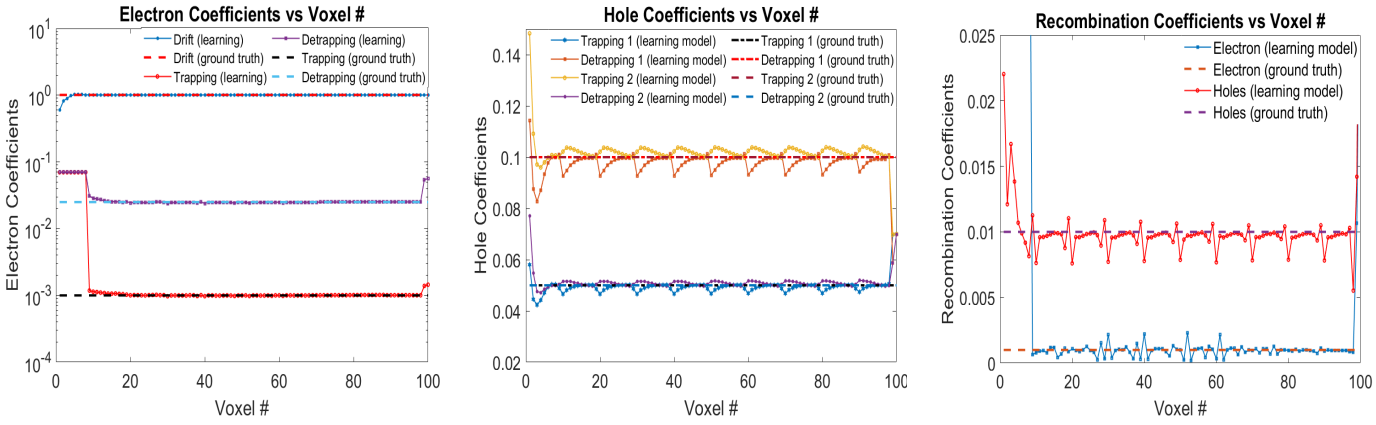

(a) (b) (c)

Fig. 13. (a) Drift coefficients (μ_e), electron coefficients ($w_{\mathrm{eT},1}$, $w_{\mathrm{eD},1}$), (b) hole coefficients ($w_{\mathrm{hT},1}$, $w_{\mathrm{hD},1}$, $w_{\mathrm{hT},2}$, $w_{\mathrm{hD},2}$), and (c) recombination coefficients ($w_{e\mathrm{Rec}}$, $w_{h\mathrm{Rec}}$) for e–h injections at voxels 9, 19, 29, 39, 49, 59, 69, 79, 89, 99 with $k = 0.1$, $l = 100$, $n = 100$. (a) Electron coefficients. (b) Hole coefficients. (c) Recombination coefficients.

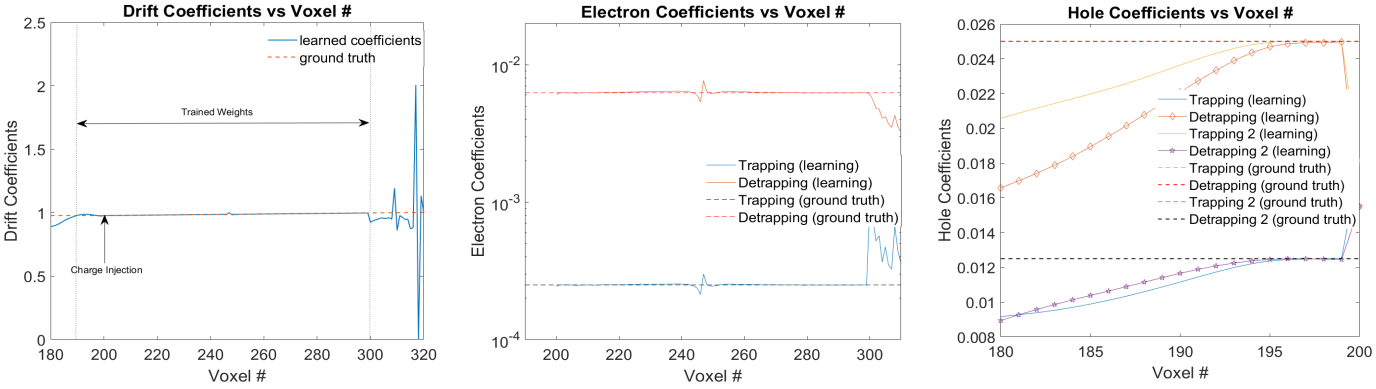

(a) (b) (c)

Fig. 14. (a) Drift coefficients (μ_e), (b) electron coefficients ($w_{\mathrm{eT},1}$, $w_{\mathrm{eD},1}$), and (c) hole coefficients ($w_{\mathrm{hT},1}$, $w_{\mathrm{hD},1}$, $w_{\mathrm{hT},2}$, $w_{\mathrm{hD},2}$), for e–h injection at Voxel 200 with $k = 0.1$, $l = 100$, $n = 100$. Readers are suggested to enlarge the figure for closer view. (a) Drift coefficients. (b) Electron coefficients. (c) Hole coefficients.

1) 400 *Voxels Model With Charge (e–h) Injection at a Particular Position:* The 400 voxels model has a time step of 2.5 ns in the ground truth model. This time step has been chosen in order to ensure that the electrons have enough time to travel from one voxel to the next adjacent voxel. Results of the model with 400 voxels with the injection of electron–hole pair at position 200 are been shown in Figs. 14 and 15. For charge injection at a particular voxel, the model was trained for 100 voxels for electron coefficients and 20 voxels for hole coefficients. $k = 0.1$, $l = 100$, and $n = 100$ were used in the loss function in (15). Clearly for the electrons and holes, the learned coefficients of drift, trapping, detrapping, and recombination match most of the ground truth values used in the MATLAB model. It must also be kept in mind that in our experiments, the weight initialization values for this model were different compared to the 100 voxels model. This is due to the fact that the ground truth parameters for this model differ from the 100 voxels model. The model coefficients for the 400 voxels model are rescaled from the 100 voxels model with a known scaling factor of $1/4$. Thus in principle, a model with any other voxel size can also be simulated with the knowledge of scaling factor. The drawback of considering finer (smaller) voxel sizes is the need for finer sampled data to train the model at the expense of added computations.

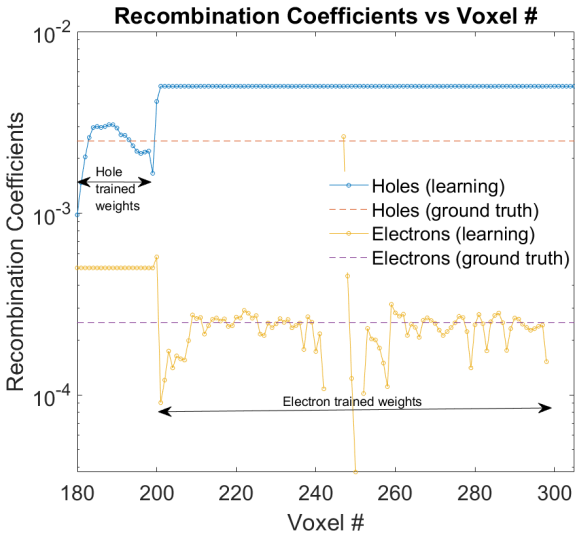

Fig. 15. Recombination coefficients for electrons and holes ($w_{e\mathrm{Rec}}$, $w_{h\mathrm{Rec}}$), for e–h injection at Voxel 200 with $k = 0.1$, $l = 100$, and $n = 100$.

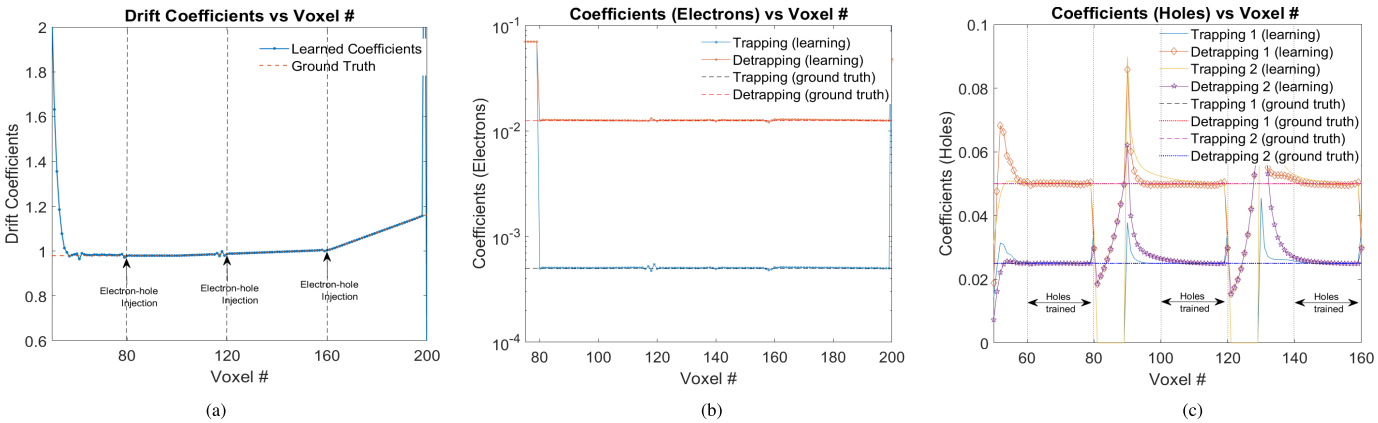

Fig. 16. (a) Drift coefficients (μ_e), (b) electron coefficients ($w_{\mathrm{eT},1}$, $w_{\mathrm{eD},1}$), and (c) hole coefficients ($w_{\mathrm{hT},1}$, $w_{\mathrm{hD},1}$, $w_{\mathrm{hT},2}$, $w_{\mathrm{hD},2}$), for multiple e–h injections at Voxel 80, 120, 160 with $k = 0.1$, $l = 100$, $n = 100$. Readers are suggested to enlarge the figure for closer view. (a) Drift coefficients. (b) Electron coefficients. (c) Hole coefficients.

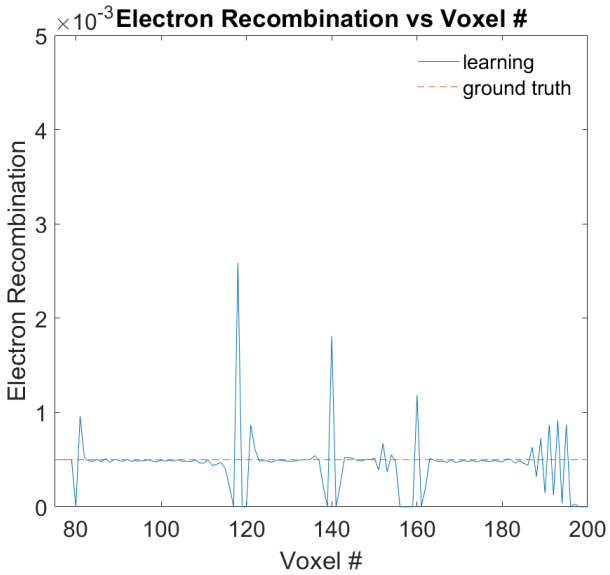

Fig. 17. Electron recombination coefficients ($w_{e\mathrm{Rec}}$) for multiple e–h injections at voxels 80, 120, 160 with $k = 0.1$, $l = 100$, $n = 100$.

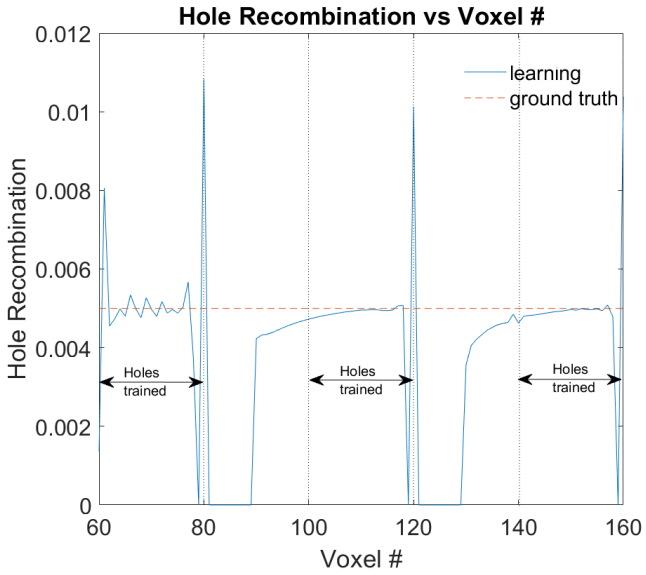

Fig. 18. Hole recombination coefficients ($w_{h\mathrm{Rec}}$) for multiple e–h injections at voxels 80, 120, 160 with $k = 0.1$, $l = 100$, $n = 100$.

2) 200 Voxels Model With Charge (e–h) Injection at Multiple Positions: The 200 voxels model has been designed with a time step of 5 ns in the ground truth model. Similar to the 400 voxel model, the parameters, if required, had to be rescaled for this model as well. The time step of 5 ns was also chosen. The results of this model with 200 voxels injected with electron–hole charges at voxel positions 80, 120 and 160 is shown in Figs. 16–18, respectively. The model is trained for 60 voxels at a time for electrons and 20 for holes. $k = 0.1$, $l = 100$ and $n = 100$ have been used in this model. Clearly, for the electrons and holes, the learned coefficients of drift, trapping, detrapping, and recombination match the ground truth values for the classical model for most of the cases. Different initializations for the model weights have been used than for the 100 voxels model. This is due to the fact that the ground truth parameters for this model differ from the 100 voxels model.

D. Comparison to Classical and Other Approaches

The current state-of-the-art approaches for determining the detector properties—drift, trapping, detrapping, and recombination of charges are typically computed using experimental methods as described in Section II. However, these approaches only characterize the material in the bulk considering the homogenous behavior of the material. On the other hand, the material properties are often nonhomogenous at a smaller length scale over the material depending on the localized doping concentration, crystalline defects and other factors. Our learning model characterizes the homogenous as well as the nonhomogenous properties of the material in terms of transport, trapping, detrapping, and recombination properties for electrons and holes at a smaller length scale over the spatial dimensions of the material compared to classical state of art methods. Thus, our method provides detailed characteristics at a smaller length scale of the material compared to the classical

experimental approaches currently in the literature. Hence, it is not meaningful to compare our method with classical approaches in the literature.

Numerically, in the voxelized model of the material, the detector parameters can be determined by exhaustive search in the parameter space. For every combination of material properties (drift, trapping, detrapping, and recombination of charges), input electron–hole charge pairs can be fed, and signals are generated at the electrodes along with free and trapped charges in each voxel of the material. On the other hand, we can obtain the signals at the electrodes and electron–hole charges (trapped and free) either from experimental data or from other theoretical models. The signals and charge distribution (free and trapped) from both of these methods can be matched by the process of matched filtering [72]. The combination of parameters can be identified which produces the best match of the signals and charges (free and trapped) for both these methods. However, the process of exhaustive search combined with matched filtering is computationally expensive. For instance, in our model with 100 voxels, each voxel has nine parameters. Considering ten discrete possible values for each of the nine parameters, the total number of possible combinations is $10^{9\times100} = 10^{900}$. Clearly, searching over all these values is very computationally expensive. Faster search algorithm such as branch and bound algorithm [73] can be used with matched filtering approach. However, all search algorithms will search from a finite set of values for the parameters. The simulation time for arriving at the model parameters will depend on the algorithm implemented. On the other hand, our learning-based modeling approach provides a gradient-based solution considering no bounds on the range of the material parameters in a reasonable time. Our learning-based model searches over an infinite range of values in the parameter space. For a single electron–hole pair input, the training time of 5 h is required. Thus, our learning-based approach provides us not only with the detailed characteristics of the material but also at a reasonable time.

Instead of the physics-inspired model, an alternative approach could be to use standard DL architectures (such as LSTM or fully connected or convolutional layers) with electron–hole pair at a position as input, and signals (at electrodes) along with free and trapped charges in the material as output corresponding to the input–output training pair. However, in such cases, the weights in the fully connected or convolutional layers do not correspond directly to the material parameters such as drift, trapping, detrapping, and recombination weights for electrons and holes. Moreover, such DL models typically have millions of trainable parameters. This not only requires a very large amount of training data, but it also requires larger training time.

VI. Discussions

The learning-based approach for obtaining the detector parameters is novel for RTSD. The model has been developed for voxels of different sizes. It learns the properties of the detector in a fast and efficient way and can identify defects in the detector spatially and their variations over time. This learning model uses error backpropagation in order to update the model parameters over the epochs. However, for a very sparse input charge pair (for example two charge inputs over a 600 voxel model), the gradients reduce for voxels away from the injection points, and hence, the model parameters are not updated effectively. This is often referred to as the vanishing gradient problem in the DL literature [74]. In order to avoid such scenarios, the incident input charges close to each other, are utilized with their corresponding outputs. In this work, we considered the physical properties of the material in terms of the number of trapped and detrapped centers for electrons and holes to be known *a priori*. Without this information, there will be an inherent model mismatch between the physical and learned model parameters, which is beyond the scope of this article.

In this work, 1-D learning model of the detector is presented. However, a 3-D learning model of the detector will follow the same principles. Moreover, in this work, the ground truth data has been simulated using a classical model described in Section III. The simulation results must be validated with actual experimental data. The experimental data can be obtained using thermoelectric emission spectroscopy, TSC measurements, laser-induced techniques, and others. However, during actual implementation of the detector, the actual signal at the electrodes along with the free and trapped charges in the material has to be used. These data will contain additional noise (such as electronic noise) which has to be modeled as well. Extending this model to work with actual experimental data in 3-D detector systems is one of the future directions of work. As a future research direction, we plan to implement a classical numerical approach and a standard DL-based algorithm for determining the properties of the RTSD. A comparative study between these techniques in terms of simulation times and computational complexity will be done in future work.

VII. Conclusion

The article introduces a novel learning-based approach to model the properties of the radiation detector material. Compared to traditional approaches, this approach aids in characterization at a smaller length scale which is not feasible with the current state-of-the-art technologies. We design the model for a CZT detector having two trapping centers for holes, one trapping center for electrons along with a recombination of electrons and holes in the bulk of the detector. Simulation experiments have been performed with an unweighted and weighted loss function to find the optimal combination of weights resulting in a minimum error for detecting the material properties. The model has been tested for 100, 200, and 400 voxels. The model shows promising results which could lead the way for future developments in RTSD.

References

[1] A. P. H. Butler *et al.*, "Bio-medical X-ray imaging with spectroscopic pixel detectors," *Nucl. Instrum. Methods Phys. Res. A, Accel. Spectrom. Detect. Assoc. Equip.*, vol. 591, no. 1, pp. 141–146, Jun. 2008.

[2] S. Leng *et al.*, "Photon-counting detector CT: System design and clinical applications of an emerging technology," *RadioGraphics*, vol. 39, no. 3, pp. 729–743, May 2019.

[3] S. K. S. Ulzheimer. (Jan. 2017). *Photon-Counting Detectors in Clinical Computed Tomography*. [Online]. Available: https://www.siemens-healthineers.com/de/computed-tomography/news/mso-photon-counting-detectors.html

[4] K. Iniewski, "CZT sensors for computed tomography: From crystal growth to image quality," *J. Instrum.*, vol. 11, no. 12, Dec. 2016, Art. no. C12034.

[5] S. A. Soldner, D. S. Bale, and C. Szeles, "Dynamic lateral polarization in CdZnTe under high flux X-ray irradiation," *IEEE Trans. Nucl. Sci.*, vol. 54, no. 5, pp. 1723–1727, Oct. 2007.

[6] D. S. Bale, S. A. Soldner, and C. Szeles, "A mechanism for dynamic lateral polarization in CdZnTe under high flux X-ray irradiation," *Appl. Phys. Lett.*, vol. 92, no. 8, Feb. 2008, Art. no. 082101.

[7] M. C. Veale *et al.*, "Characterization of the uniformity of high-flux CdZnTe material," *Sensors*, vol. 20, no. 10, p. 2747, May 2020.

[8] M. D. Wilson *et al.*, "A 10 cm×10 cm CdTe spectroscopic imaging detector based on the HEXITEC ASIC," *J. Instrum.*, vol. 10, no. 10, Oct. 2015, Art. no. P10011.

[9] P. Zambon *et al.*, "Spectral response characterization of CdTe sensors of different pixel size with the IBEX ASIC," *Nucl. Instrum. Methods Phys. Res. A, Accel. Spectrom. Detect. Assoc. Equip.*, vol. 892, pp. 106–113, Jun. 2018.

[10] M. Z. Alom *et al.*, "The history began from AlexNet: A comprehensive survey on deep learning approaches," 2018, *arXiv:1803.01164*.

[11] Y. LeCun, L. Bottou, Y. Bengio, and P. Haffner, "Gradient-based learning applied to document recognition," *Proc. IEEE*, vol. 86, no. 11, pp. 2278–2324, Nov. 1998.

[12] A. Krizhevsky, I. Sutskever, and G. E. Hinton, "Imagenet classification with deep convolutional neural networks," in *Proc. Adv. Neural Inf. Process. Syst.*, vol. 25, 2012, pp. 1097–1105.

[13] K. Simonyan and A. Zisserman, "Very deep convolutional networks for large-scale image recognition," 2014, *arXiv:1409.1556*.

[14] F. A. Gers and J. Schmidhuber, "Recurrent nets that time and count," in *Proc. IEEE-INNS-ENNS Int. Joint Conf. Neural Netw. (IJCNN)*, vol. 3, Jul. 2000, pp. 189–194.

[15] F. A. Gers, N. N. Schraudolph, and J. Schmidhuber, "Learning precise timing with LSTM recurrent networks," *J. Mach. Learn. Res.*, vol. 3, no. 1, pp. 115–143, 2002.

[16] I. J. Goodfellow *et al.*, "Generative adversarial networks," 2014, *arXiv:1406.2661*.

[17] A. Lucas, M. Iliadis, R. Molina, and A. K. Katsaggelos, "Using deep neural networks for inverse problems in imaging: Beyond analytical methods," *IEEE Trans. Signal Process. Mag.*, vol. 35, no. 1, pp. 20–36, Jan. 2018.

[18] A. Lucas, S. López-Tapia, R. Molina, and A. K. Katsaggelos, "Generative adversarial networks and perceptual losses for video super-resolution," *IEEE Trans. Image Process.*, vol. 28, no. 7, pp. 3312–3327, Jul. 2019.

[19] P. Besson, T. Parrish, A. K. Katsaggelos, and S. K. Bandt, "Geometric deep learning on brain shape predicts sex and age," *Comput. Med. Imag. Graph.*, vol. 91, Jul. 2021, Art. no. 101939.

[20] B. Thomas, M. C. Veale, M. D. Wilson, P. Seller, A. Schneider, and K. Iniewski, "Characterisation of redlen high-flux CdZnTe," *J. Instrum.*, vol. 12, no. 12, Dec. 2017, Art. no. C12045.

[21] E. Y. Lee, R. B. James, R. W. Olsen, and H. Hermon, "Compensation and trapping in CdZnTe radiation detectors studied by thermoelectric emission spectroscopy, thermally stimulated conductivity, and current-voltage measurements," *J. Electron. Mater.*, vol. 28, no. 6, pp. 766–773, Jun. 1999.

[22] G. C. Tepper, R. Kessick, R. B. James, and L. Van den Berg, "Contactless measurements of charge traps and carrier lifetimes in detector-grade cadmium zinc telluride and mercuric iodide," *Proc. SPIE*, vol. 4141, pp. 76–88, Nov. 2000.

[23] Z. Medunić, Ž. Pastuović, M. Jakšić, and N. Skukan, "Studying of trap levels by the use of focused ion beams," *Nucl. Instrum. Methods Phys. Res. Sect. B, Beam Interact. Mater. At.*, vol. 231, nos. 1–4, pp. 486–490, Apr. 2005.

[24] G. C. Tepper, R. Kessick, and C. Szeles, "Investigation of the electronic properties of cadmium zinc telluride surfaces using pulsed laser microwave cavity perturbation," *Proc. SPIE*, vol. 4507, pp. 79–89, Dec. 2001.

[25] M. Pavlović, M. Jakšić, H. Zorc, and Z. Medunić, "Identification of deep trap levels from thermally stimulated current spectra of semi-insulating CdZnTe detector material," *J. Appl. Phys.*, vol. 104, no. 2, Jul. 2008, Art. no. 023525.

[26] R. Nan, W. Jie, G. Zha, B. Wang, Y. Xu, and H. Yu, "Irradiation-induced defects in $Cd_{0.9}Zn_{0.1}Te$: Al," *J. Electron. Mater.*, vol. 41, no. 11, pp. 3044–3049, 2012.

[27] M. L. Rodrigues and Z. He, "High-flux experiments and simulations of pulse-mode 3D-position-sensitive CdZnTe pixelated detectors," in *Proc. IEEE Nucl. Sci. Symp. Conf. Rec.*, Oct. 2011, pp. 4677–4688.

[28] K. Hecht, "Zum mechanismus des lichtelektrischen primärstromes in isolierenden kristallen," *Zeitschrift Physik*, vol. 77, nos. 3–4, pp. 235–245, 1932.

[29] K. S. Shah, J. C. Lund, and F. Olschner, "Charge collection efficiency in a semiconductor radiation detector with a non-constant electric field," *IEEE Trans. Nucl. Sci.*, vol. 37, no. 2, pp. 183–186, Apr. 1990.

[30] Y. Nemirovsky, A. Ruzin, G. Asa, and J. Gorelik, "Study of the charge collection efficiency of CdZnTe radiation detectors," *J. Electron. Mater.*, vol. 25, no. 8, pp. 1221–1231, Aug. 1996.

[31] Y. Nemirovsky, "Statistical modeling of charge collection in semiconductor gamma-ray spectrometers," *J. Appl. Phys.*, vol. 85, no. 1, pp. 8–15, Jan. 1999.

[32] M. Ifraimov, A. Ludwig, and Y. Nemirovsky, "Statistical modeling of the spectral performance of a two-dimensional array of gamma-ray spectrometers," *J. Appl. Phys.*, vol. 91, no. 5, pp. 3384–3397, Mar. 2002.

[33] R. Blakney and H. Grunwald, "Small-signal current transients in insulators with traps," *Phys. Rev.*, vol. 159, no. 3, p. 658, 1967.

[34] K. R. Zanio, W. M. Akutagawa, and R. Kikuchi, "Transient currents in semi-insulating CdTe characteristic of deep traps," *J. Appl. Phys.*, vol. 39, no. 6, pp. 2818–2828, May 1968.

[35] G. Juška, A. Matulionis, and J. Viščakas, "Measurement of thermal release and transit time in case of multiple trapping," *Phys. Status Solidi B*, vol. 33, no. 2, pp. 533–539, 1969.

[36] M. Jung, J. Morel, P. Fougeres, M. Hage-Ali, and P. Siffert, "A new method for evaluation of transport properties in CdTe and CZT detectors," *Nucl. Instrum. Methods Phys. Res. A, Accel. Spectrom. Detect. Assoc. Equip.*, vol. 428, no. 1, pp. 45–57, 1999.

[37] M. Prokesch, D. S. Bale, and C. Szeles, "Fast high-flux response of CdZnTe X-ray detectors by optical manipulation of deep level defect occupations," *IEEE Trans. Nucl. Sci.*, vol. 57, no. 4, pp. 2397–2399, Aug. 2010.

[38] Q. Zheng *et al.*, "Investigation of generation of defects due to metallization on CdZnTe detectors," *J. Phys. D, Appl. Phys.*, vol. 45, no. 17, May 2012, Art. no. 175102.

[39] L. Xu *et al.*, "Effects of deep-level defects on carrier mobility in CdZnTe crystals," *Nucl. Instrum. Methods Phys. Res. A, Accel. Spectrom. Detect. Assoc. Equip.*, vol. 767, pp. 318–321, Dec. 2014.

[40] Y. Zaman *et al.*, "Characterization of CdZnTe co-doped with indium and lead," *Nucl. Instrum. Methods Phys. Res. A, Accel. Spectrom. Detect. Assoc. Equip.*, vol. 770, pp. 48–51, Jan. 2015.

[41] J. Willard, X. Jia, S. Xu, M. Steinbach, and V. Kumar, "Integrating scientific knowledge with machine learning for engineering and environmental systems," 2020, *arXiv:2003.04919*.

[42] L.-F. Arsenault, A. Lopez-Bezanilla, O. A. von Lilienfeld, and A. J. Millis, "Machine learning for many-body physics: The case of the Anderson impurity model," *Phys. Rev. B, Condens. Matter*, vol. 90, no. 15, Oct. 2014, Art. no. 155136.

[43] K. Rudd and S. Ferrari, "A constrained integration (CINT) approach to solving partial differential equations using artificial neural networks," *Neurocomputing*, vol. 155, pp. 277–285, May 2015.

[44] Y. Khoo, J. Lu, and L. Ying, "Solving for high-dimensional committor functions using artificial neural networks," *Res. Math. Sci.*, vol. 6, no. 1, p. 1, Mar. 2019.

[45] J. Han, E. Weinan, and A. Jentzen, "Solving high-dimensional partial differential equations using deep learning," *Proc. Nat. Acad. Sci. USA*, vol. 115, no. 34, pp. 8505–8510, 2018.

[46] A. H. Vija *et al.*, "Physics-constrained network and training thereof," U.S. Patent 15 929 502, Apr. 15 2021.

[47] P. Ritt, K. Seidl, M. Cachovan, A. Vija, and T. Kuwert, "Data-driven respiratory spect-gating for determination of liver-lung-shunt fraction," *Nuklearmedizin*, vol. 60, no. 2, p. P14, 2021.

[48] J. C. Sanders and A. H. Vija, "Data-driven surrogate respiratory signal generation for medical imaging," U.S. Patent 10 292 671, May 21 2019.

[49] T. Hamilton and H. Mohseni, "Space-time scattering network for electromagnetic inverse design and tomography," 2018, *arXiv:1811.07207*.

[50] E. Diéguez, "Growth of $Cd_{0.9}Zn_{0.1}Te$ bulk crystals," in *Comprehensive Semiconductor Science and Technology*, vol. 3. Amsterdam, The Netherlands: Elsevier, 2011, ch. 3.04, pp. 170–201.

[51] W. Shockley and W. T. Read, "Statistics of the recombinations of holes and electrons," *Phys. Rev.*, vol. 87, p. 835, Sep. 1952.

[52] R. N. Hall, "Electron-hole recombination in germanium," *Phys. Rev.*, vol. 87, no. 2, p. 387, 1952.

[53] M. Rodrigues and Z. He, "Properties and spectroscopic performance of semiconductor detectors under high-flux irradiation," *Proc. SPIE*, vol. 8143, Sep. 2011, Art. no. 81430A.

[54] T. H. Prettyman, "Method for mapping charge pulses in semiconductor radiation detectors," *Nucl. Instrum. Methods Phys. Res. A, Accel. Spectrom. Detect. Assoc. Equip.*, vol. 422, nos. 1–3, pp. 232–237, Feb. 1999.

[55] J. Durst, P. Bartl, B. Kreisler, T. Michel, and G. Anton, "Monte Carlo simulation of pixelated photon counting X-ray detectors like the Medipix2 and the Medipix3 using high-Z sensor materials," in *Proc. IEEE Nucl. Sci. Symp. Conf. Rec.*, Oct. 2008, pp. 4990–4994.

[56] M. Ruat, E. G. d'Aillon, and L. Verger, "3D semiconductor radiation detectors for medical imaging: Simulation and design," in *Proc. IEEE Nucl. Sci. Symp. Conf. Rec.*, Oct. 2008, pp. 434–439.

[57] M. Picone, A. Glière, and P. Massé, "A three-dimensional model of CdZnTe gamma-ray spectrometer," *Nucl. Instrum. Methods Phys. Res. A, Accel. Spectrom. Detect. Assoc. Equip.*, vol. 504, nos. 1–3, pp. 313–316, May 2003.

[58] V. I. Kolobov, "Fokker–Planck modeling of electron kinetics in plasmas and semiconductors," *Comput. Mater. Sci.*, vol. 28, no. 2, pp. 302–320, Oct. 2003.

[59] S. M. Sze and K. K. Ng, *Physics of Semiconductor Devices*. Hoboken, NJ, USA: Wiley, 2006.

[60] M. Rodrigues, "High-flux experiments and simulations of pulse-mode position-sensitive CdZnTe pixelated detectors," Ph.D. dissertation, Dept. Nucl. Eng. Radiological Sci., Univ. Michigan, Ann Arbor, MI, USA, 2012.

[61] M. Prokesch, "CdZnTe for gamma and X-ray applications," *Solid-State Radiation Detectors: Technology and Applications*. Boca Raton, FL, USA: CRC Press, 2015, pp. 17–48.

[62] W. Shockley, "Currents to conductors induced by a moving point charge," *J. Appl. Phys.*, vol. 9, no. 10, pp. 635–636, 1938.

[63] S. Ramo, "Currents induced by electron motion," *Proc. IRE*, vol. 27, no. 9, pp. 584–585, Sep. 1939.

[64] H. Spieler, *Semiconductor Detector Systems*. Oxford, U.K.: Oxford Univ. Press, 2005, vol. 12.

[65] G. F. Knoll, *Radiation Detection and Measurement*. Hoboken, NJ, USA: Wiley, 2010.

[66] Z. He, "Review of the Shockley–Ramo theorem and its application in semiconductor gamma-ray detectors," *Nucl. Instrum. Methods Phys. Res. A, Accel. Spectrom. Detect. Assoc. Equip.*, vol. 463, nos. 1–2, pp. 250–267, 2001.

[67] G. Van Houdt, C. Mosquera, and G. Nápoles, "A review on the long short-term memory model," *Artif. Intell. Rev.*, vol. 53, no. 8, pp. 5929–5955, Dec. 2020.

[68] D. E. Rumelhart, G. E. Hinton, and R. J. Williams, "Learning internal representations by error propagation," California Univ San Diego La Jolla Inst. Cognitive Sci., La Jolla, CA, USA, ICS Rep. 8506, 1985.

[69] P. J. Werbos, "Backpropagation through time: What it does and how to do it," *Proc. IEEE*, vol. 78, no. 10, pp. 1550–1560, Oct. 1990.

[70] D. P. Kingma and J. Ba, "Adam: A method for stochastic optimization," 2014, *arXiv:1412.6980*.

[71] M. Abadi, A. Agarwal, P. Barham, E. Brevdo, Z. Chen, and C. Citro. (2015). *TensorFlow: Large-Scale Machine Learning on Heterogeneous Systems*. [Online]. Available: https://www.tensorflow.org/

[72] G. B. Giannakis and M. K. Tsatsanis, "Signal detection and classification using matched filtering and higher order statistics," *IEEE Trans. Acoust., Speech Signal Process.*, vol. 38, no. 7, pp. 1284–1296, Jul. 1990.

[73] D. R. Morrison, S. H. Jacobson, J. J. Sauppe, and E. C. Sewell, "Branch-and-bound algorithms: A survey of recent advances in searching, branching, and pruning," *Discrete Optim.*, vol. 19, pp. 79–102, Feb. 2016.

[74] S. Hochreiter, "The vanishing gradient problem during learning recurrent neural nets and problem solutions," *Uncertain. Fuzziness Knowl.-Based Syst.*, vol. 6, no. 2, pp. 107–116, 1998.